Texas A&M University
Mechanical Engineering Department
Turbomachinery Laboratory
Tribology Group

Further Imbalance Response Measurements of Rotor Supported on Bump-Type Gas Foil Bearings: Operation to 50 krpm

Research Progress Report to the TAMU Turbomachinery Research Consortium

TRC-B&C-2-06

by

Luis San Andrés

Mast-Childs Professor

Principal Investigator

Tae Ho Kim

Research Assistant

June 2006

This material is based upon work supported by the National Science Foundation under Grant No. 0322925

Gas Foil Bearings for Oil-Free Rotating Machinery – Analysis Anchored to Experiments
NSF Funded Project, TEES # 32525/53900/ME

EXECUTIVE SUMMARY

A 2005 TRC report presents imbalance response measurements of a hollow test rotor supported on bump-type gas foil bearings. The top speed of the tests is 25 krpm, the limit of the drive router motor. The 2005 measurements show the gas foil bearings are prone to subsynchronous whirl with amplitudes of motion exacerbated by the imbalance condition of the rotor, i.e. a forced nonlinearity. Presently, a 0.75 kW (1 HP) motor with maximum speed of 50 krpm drives the rotor through a flexible coupling. However, at start up the AC motor does not have enough torque to overcome the dry-friction from the foil bearings contacting the rotor. Hence, the original DC router motor, 1.49 kW (2.0 HP), is installed on the free end of the motor with a centrifugal clutch that engages the test rotor, overcomes the friction in the bearings and accelerates the rotor towards high speeds. The router motor is turned off and the main drive motor spins the test rotor to a top speed of 50 krpm. The rotor is balanced first in a commercial machine and then in-place; the maximum motion amplitudes are less than 12 μm, ~ 27 % of the nominal bearing clearance (c = 45 μm), in the speed range from 2 to 25 krpm.

Coast down rotor responses from 50 krpm to rest are recorded only for the baseline imbalance condition and with side pressurization into the bearings set at 0.34 bar (5 psig). The test data show significant subsynchronous motions from 50 krpm to 27 krpm with a main whirl frequency ranging from 20 % to 27% of rotor speed. At lower rotor speeds, subsynchronous motions are negligible. The rotor speed decay curve versus time is linear from 50 krpm to 30 krpm, and from 5 krpm to rest, thus implying rotor rubbing. From 30 krpm towards 5 krpm, the speed decay is exponential showing operation with a gas film in the foil bearings.

Measurements of rotor motion are obtained for increasing imbalance masses, in-phase and out-of-phase, in coast down tests from 25 krpm where no subsynchronous vibrations exist. The amplitudes of synchronous motion show passage through a critical speed that decreases from 13 krpm to 9 krpm as the imbalance mass increases. The peak amplitudes of motion appear to increase proportionally with the imbalance, thus giving some assurance into the linearity of the test rotor-gas foil bearing system. A rotordynamic analysis to predict the measurements is presently being conducted. In spite of the large motions recorded for speeds above 26 krpm when subsynchronous whirl sets in, the gas foil bearings tolerated without damage a persistent rubbing condition. Thus, the experimental results confirm gas foil bearings are more rugged and reliable than other types of gas bearings operating under similar test conditions.

TABLE OF CONTENTS

LIST OF TABLES

LIST OF FIGURES

NOMENCLATURE

c	Foil bearing radial clearance [μm]
DV, DH	Drive end bearing, vertical and horizontal planes
FV, FH	Free end bearing, vertical and horizontal planes
m_e	Mass imbalance [m]
M	Rotor mass [kg]
N	Rotor speed [rpm]
r	Radius for imbalance mass [m]
U_{max}	Allowable maximum residual imbalance, $4W/N$ for API standard [oz-inch]
u	$m_e r/M$, Imbalance displacement [μm]
W	Rotor weight [lb_f]
X, Y	Horizontal and vertical rotor displacements
WFR	Whirl frequency ratio
ξ	Damping ratio
Ω	Rotor angular speed [rad/s]
$\Omega_{threshold}$	Threshold speed of instability [rad/s]

I. INTRODUCTION

Implementing gas foil bearings (GFBs) in micro turbomachinery to 0.2 MW reduces system complexity and maintenance costs, while increasing its efficiency and operating life [1, 2]. GFBs are compliant-surface (self-acting) hydrodynamic bearings that use ambient air or any process gas as the lubricating fluid. A hydrodynamic film pressure builds up within the small gap between the rotating shaft and the smooth foil deflects the compliant bearing surface, thus reducing friction and providing load support. A GFB's forced performance depends upon the material properties and geometrical configuration of the support structure (top foil and bumps strip layers), as well as the hydrodynamic film pressure built within the bearing clearance. Material hysteresis and dry-frictional dissipation mechanisms between the bumps and top foil, as well as the bumps and the bearing inner surface, act to enhance the bearing damping ability [3].

In comparison to rolling element bearings, GFBs demonstrate superior reliability in Air Cycle Machines (ACMs) of Aircraft Environmental Control Systems (ECSs) [4-6]. Decades of applied research show that corrugated bump GFBs fulfill most of the requirements of highly efficient oil-free turbomachinery, with ultimate load capacity up to 680 kPa (100 psi) [7,8].

Figure 1 shows the configurations of the test GFB. The corrugated bumps, when loaded, offer an increasing structural stiffness, and dry-friction between the bumps and top foil and the bumps and the bearing inner surface provide a mechanism for damping.

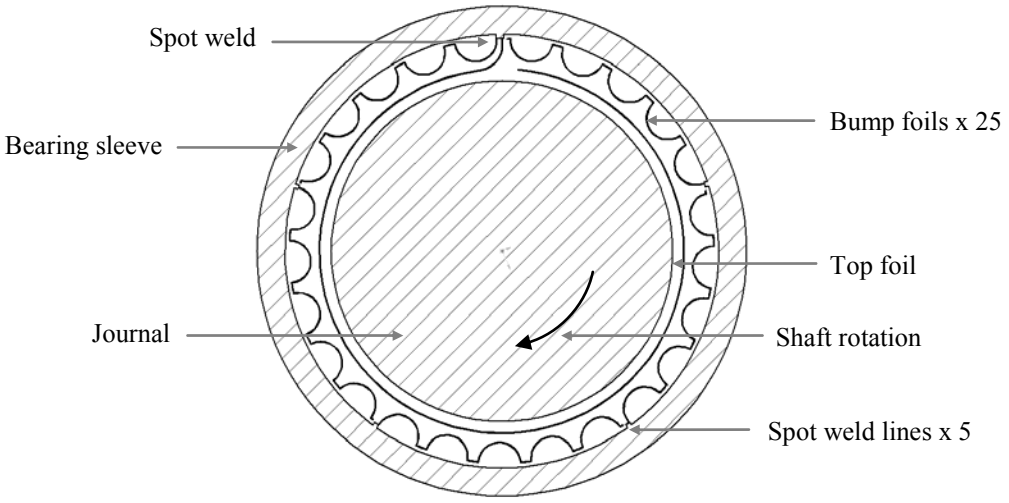

Figure 1. Schematic representation of a bump-type gas foil bearing

In spite of the extensive industrial usage of GFBs including various applications as micro turbines [1], turbo compressors [9], and turbo blowers [10], there is no reliable experimental test data on the rotordynamic performance of a rotor supported on GFBs. This limitation has delayed the implementation of GFBs into high performance turbomachinery systems such as in small gas turbine engines, for example [7].

This report presents imbalance response test results up to 50 krpm, aiming to identify regions of stable and unstable rotordynamic response for various imbalance conditions. The test data will serve to validate predictions form a computational model.

II. PAST WORK

Ruscitto et al. [12] perform a series of load capacity tests on first generation bump type foil bearings [7]. The test bearing, 38 mm in diameter and 38 mm in length, has a single top foil and a single bumps' strip layer. The authors note that the actual bearing clearance for the test bearing is unknown. Thus, the journal radial travel (c_J) was measured by performing a static load-bump deflection test. The authors installed displacement sensors inside the rotor and measured the gap between the rotor and the top foil at the bearing's center plane and near the bearing edge. As the static load increases, for a fixed rotational speed, the minimum film thickness and journal attitude angle decrease exponentially. As the applied load increased, the journal eccentricity grows proportionally and does not depend on the journal rotational speed. The test data for film thickness is the only one available in the open literature.

Heshmat et al. [13] test two types of second generation [7] bump type GFBs: one with a single top foil (360 degrees in extent), and the other with three shorter top foils spanning the bearing circumference. The bearings are 35mm in diameter and 44 mm in width. The top foils rest on single split-staggered bump layer strips. To improve frictional characteristics, the underneath surfaces of the top foils are sputter coated with copper. Static load versus deflection tests show that the three-foil bearing has a varying structural stiffness; largest near the weld of the bump strip layer, and smallest near the free end of the bump layer. Rotordynamic measurements show that the multiple-foil gas bearings are more stable than the bearing with a single foil covering the entire bearing circumference. Four levels of in-phase unbalance rotor tests show that the onset speed for appearance of subsynchronous whirl large amplitude motions is, to some degree, inversely proportional to the magnitude of the mass imbalance level. The single-foil bearing with the copper

coating operated to a top speed of 120 krpm and supported, at 68 krpm, an ultimate static load of 534 N (120 lb) [352 kPa (51 psi) specific load] .

Heshmat [8] introduces single foil, multistage bump strip layers to engineer tunable bearing support stiffness along the radial and circumferential directions. The designed stiffness gradient ensures a hydrodynamic wedge or a lobe-like effect for enhanced generation of hydrodynamic pressure. As the shaft speed increases, gas pressure pushes the top foil and bumps outwards, automatically forming a converging wedge film shape. In the experiments, a multistage bump strips GFB of 35 mm in diameter and 31 mm in length achieves an impressive ultimate load capacity of 728 N [6.73 bar (98 psi) specific pressure]. Heshmat also demonstrates the successful operation of foil bearings to a maximum speed of 132 krpm, i.e. 4.61×10^6 DN value, albeit the vibration measurements show large amplitude subsynchronous whirl motions related to the test rotor rigid body mode natural frequencies. However, in spite of the subsynchronous whirl, the rotor reached a stable limit cycle operation.

Childs disputes the conclusions in [8] and warns against additional destabilizing forces from seal elements and aerodynamic effects in a turbine, for example. Incidentally, one other concern relates to the effective viscous damping, derived from dry-friction, which is inversely proportional to both amplitude and frequency of shaft motion.

Heshmat [14] demonstrates the operation of a flexible rotor supported on GFBs beyond its first bending mode critical speed The rotor imbalance responses are purely synchronous for speeds before passing the rotor bending critical speed of 34 krpm. Then, large subsynchronous vibrations at the rigid body mode (low) natural frequency appear while passing the bending critical speed and continuing to speed up to 85 krpm. Nevertheless, the recorded imbalance responses show no evidence of severe rotordynamic instability since limit cycle orbits are apparent.

Lee et al. [15] introduce a viscoelastic-bump foil bearing to improve the damping characteristics of GFBs. Structural tests using shakers demonstrate that the viscoelastic-bump foil bearing offers a larger equivalent viscous damping than a simpler GFB with one layer of 5 μm – copper - coated bump foils. A series of super critical bending mode operations of the rotor supported on the two different types of GFBs reveals that the viscoelastic-bump foil bearings not only aids in attenuating the large amplitudes of

motion near the rotor bending critical speed, but also suppress subsynchronous motions at rotor speeds higher than the rotor bending critical speed.

Howard et al. [16] perform impact tests on a GFB and characterize its dynamic direct stiffness and damping coefficients for operation at various temperatures, loads and speed conditions. Cross-coupled stiffness and damping were not identified in the test procedure. Transient response calculations using experimentally derived bearing parameters are compared with both exponential (viscous damping) and linear (Coulomb damping) motion amplitude decays to find the dominant mode of energy dissipation. Experimental results demonstrate that at high temperatures and low static loads, the gas film is soft (compared to the foil structure) thus showing viscous damping behavior. Conversely, at low temperatures and high static loads the bearing behaves like a dry friction system since the gas film becomes stiffer than the foil structure.

Recently, San Andrés et al. [17] investigate the rotordynamic performance of a rotor supported on GFBs. A series of coastdown tests with small to large imbalance masses inserted in a hollow rotor demonstrate that GFBs have nonlinear rotordynamic characteristics; large imbalance masses induce subsynchronous motions of large amplitude and associated with low frequency rigid body modes. Rotordynamic model predictions do not correlate well with the test data. A comparison of normalized imbalance response amplitudes reveals a nonlinear rotor behavior since the GFB stiffness and damping coefficients are apparently amplitude and frequency dependent. External air pressurization through the bearing ends aids to reduce the amplitude of synchronous motions while crossing a critical speed. Incidentally, the tests also demonstrate that increasing air pressurization ameliorates the amplitudes of subsynchronous motions due to the significant effect of the axial flow retarding the circumferential flow development within the gas bearings.

III. DESCRIPTION OF TEST FOIL BEARINGS AND EXPERIMENTAL TEST FACILITY

Figure 2 shows the test GFBs acquired from Foster-Miller Technologies and a test rotor, consisting of a hollow shaft 209.5 mm in length and 38.10 mm in diameter at the bearing locations [18]. Table 1 displays the geometry and properties of the test GFBs and rotor. The GFBs consist of five arcuate bump strips, each with five bumps. The end of a strip is welded to the bearing sleeve, while the other end is free. The top foil, coated with a spray-on Teflon® type coating of thickness 25.4 μm, consists of a thin metal sheet welded at the bearing sleeve at one end (spot welded), and free at the other end. A thin, dense, chrome layer thickness 25.4 μm coats the rotor surface where the bearings are located. The coating acts to reduce friction and wear at the rotor - top foil interface. The rotor drive and free ends have 8 threaded holes at a 15.11 mm radius, where imbalance masses are added.

Figure 3 shows the GFB test rig for the rotordynamic experiments. A steel housing holds the foil bearings and contains an internal duct to supply air pressure up to 7 bars (100 psig) for cooling the bearings, if needed. A 0.75 kW (1 HP) DC electric motor with maximum speed of 50 krpm drives the test rotor through a flexible coupling and quill shaft. The DC motor torque is not large enough to overcome the stall torque at rotor start-up. Hence, a router AC motor, 1.49 kW (2.0 HP) with maximum speed of 25 krpm, is used to assist the rotor start up speed through a centrifugal clutch connected on the hollow side of the test rotor.

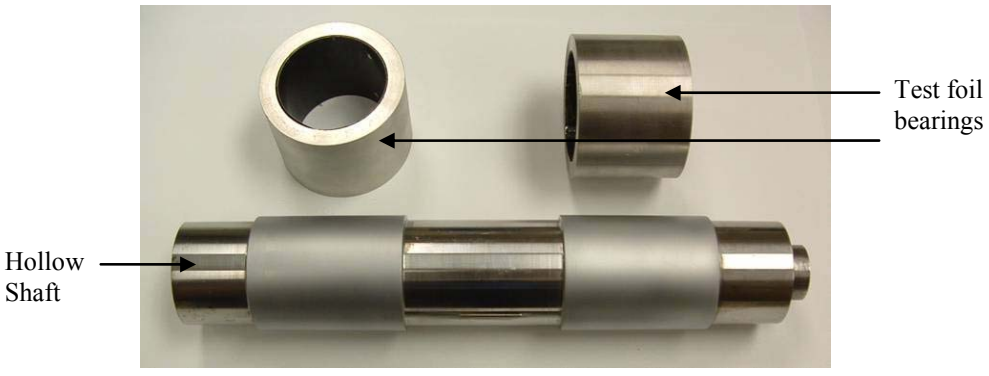

Figure 2. Test rotor and foil bearings for rotordynamic tests [18]

Table 1 Geometry and properties of test GFBs and rotor [18]

***GFB* Parameters:** 25 bumps	SI Units
Bearing inner diameter, D	38.10 mm
Axial bearing length, L	38.10 mm
Bump pitch, p	4.572 mm
Bump length, l_o	4.064 mm
Foil thickness, t	0.102 mm
Bump height, h	0.381 mm
Poisson's ratio, v	0.29
Bump modulus of elasticity, E	213 GPa
Bearing mass, M_B	0.27 kg
Free-free end bump stiffness, K_F	0.526 MN/m
Free-fixed bump stiffness, K_W	0.876 MN/m
Rotor Parameters	
Rotor modulus of elasticity, E_R	193 GPa
Material density, ρ	7830 kg/m^3
Total mass, M	0.98 kg
Diameter at the bearing locations, D_j with thin chrome coating	38.20 mm
Total length, L_T	209.55 mm
Distance between bearing locations, L_S	100.58 mm
Distance between rotor CG to free end, x_G	125.73 mm
Transverse moment of inertia, I_T	37.1 kg.cm^2
Polar moment of inertia, I_P	2.24 kg.cm^2
Coupling lateral stiffness	1.63×10^5 N/m

The uncertainties on physical dimensions are within 3%,
Bump stiffnesses estimated using Iordanoff formulas [19].

The clutch has three shoes hinged on a disk and preloaded with a circular spring element. The spring restricts the clutch shoes from expanding at null rotor speed. The centrifugal clutch is accurately positioned inside a wear ring press-fitted into the free end of the hollow rotor. The wear ring (soft material) prevents damage of the clutch shoes and the inner surface of the test rotor when in contact. Upon assembly, a diametrical clearance of ~ 1 mm is maintained between the clutch shoes and the inner surface of the wear ring. The drive motor and router motor are turned on simultaneously, and the clutch shoes begin to expand as the router motor speed increases, contact and engage the wear

ring and the test rotor begins to spin. Once the test rotor lifts off from its bearing the drag torque decreases because of the generation of the hydrodynamic gas film in the foil bearings and the router motor is manually turned off, decelerating to rest while the clutch shoes close and disengaged at approximately 5 krpm.

An infrared tachometer records the rotor speed, and two pairs of orthogonally positioned eddy current sensors located at both rotor ends record the lateral rotor motions along the horizontal and vertical planes.

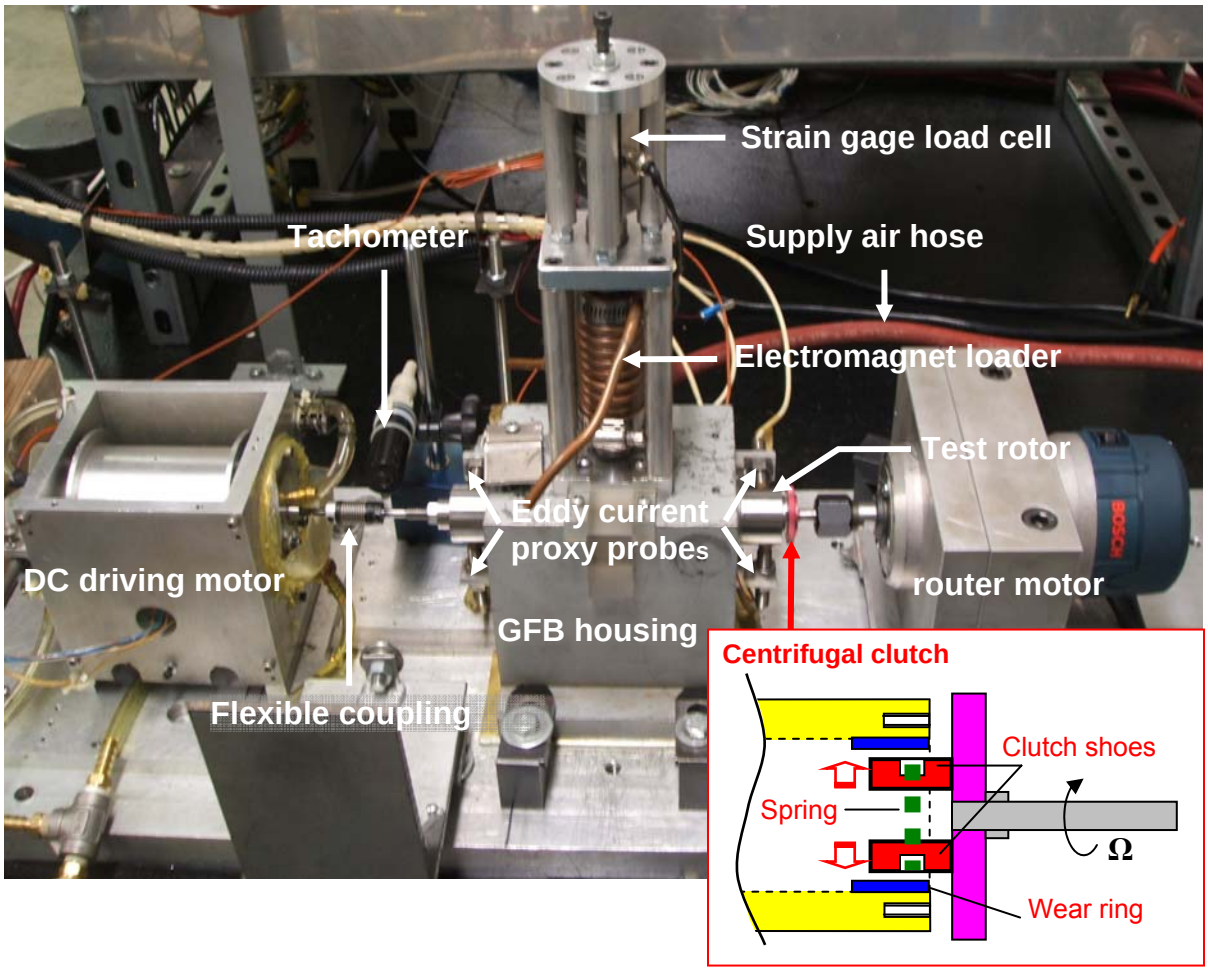

Figure 3. Test rig for rotordynamic tests of a rotor supported on *GFB*s

Figure 4 shows a layout of the GFB test rig setup and its instrumentation. Rotor dynamic displacement signals from the eddy current sensors connect to a signal conditioner to bias their DC offset levels and routed into a commercial DAQ system for machinery monitoring and diagnostics. A two-channel dynamic signal analyzer displays the frequency content of the selected motion signals, and analog oscilloscopes display the

unfiltered rotor orbits in real time. While operating the test rig, the temperatures on the outer surfaces of the test foil bearings and the drive motor are also recorded.

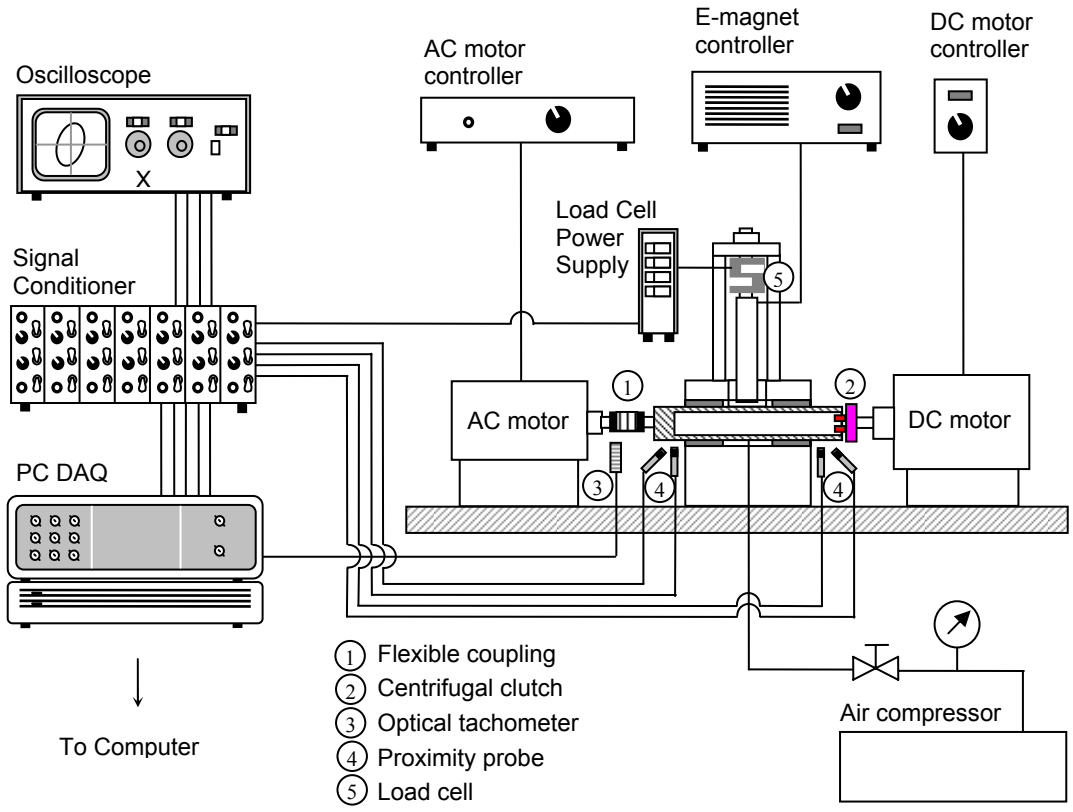

Figure 4. Layout of GFB test rig setup and instrumentation

The test rotor was first balanced in a commercial balancing machine. Trim balancing in place followed with application of the two plane influence coefficient method [20]. The resultant maximum total motions at the rotor drive end and free end bearings are less than 24 μm, i.e., 27 % of the nominal bearing diametrical clearance, for operation between 2 krpm and 25 krpm.

IV. ROTORDYNAMIC PERFORMANCE OF ROTOR SUPPORTED ON TEST GFBS

IV.1 COAST DOWN ROTOR RESPONSES FROM 50 KRPM AND BASELINE IMBALANCE CONDITION

A rotor coast down speed test from 50 krpm was conducted with feed air pressure at 34.5 kPa (5 psi) and the rotor at its baseline imbalance condition, Figure 5 displays waterfall plots of vertical motions recorded at the rotor free and drive ends. The horizontal axes depict the frequency content of the motions, whose amplitudes are depicted along the vertical axes. Subsynchronous motions of large amplitude are evident from 50 krpm to 27 krpm. For lower rotor speeds, the motion is mainly synchronous.

Figure 6 presents the FFT of the rotor motion at its free end (vertical plane) for operation at 50 krpm. The amplitude of subsynchronous motion, 56 μm (0-pk) at 180 Hz, is much larger than the synchronous component, 4 μm (0-pk) at 830 Hz.

Figure 7 presents the analysis of the frequency content, synchronous and subsynchronous, and amplitudes of motion versus rotor speed. The amplitudes of synchronous motion are smaller than 6 μm (0-pk) over the whole speed range. On the other hand, the amplitudes of subsynchronous motion are much larger, decreasing slightly as the rotor decelerates. Most importantly, the subsynchronous whirl disappears suddenly at a speed of 27 krpm. The subsynchronous whirl frequency decreases from 180 Hz to 125 Hz as the rotor coasts down from 50 krpm to 27 krpm. Figure 7 also shows the whirl frequency ratio (*WFR*), i.e. the ratio of whirl frequency to rotor angular frequency, increasing from 0.20 to 0.27 at rotor speed equal to 26 krpm. For lower rotor speeds, no major subsynchronous motions are recorded.

The rotor is rigid for the speed range tested; and hence, rotor motions at the location of the bearings can be easily estimated using simple arithmetic rules. Figure 8 displays the rotor orbits (with DC offset subtraction) at three shaft speeds. In all cases, the whirl orbital motion is forward, i.e. in the direction of rotor speed. At 50 krpm, the peak to peak amplitudes of shaft motion are ~ 200 μm, slightly larger than the bearings' diametric

clearances (90 μm and 100 μm for the drive end and free end bearings, respectively). At 26 krpm, the amplitude of motion is slightly smaller than the bearings' clearances. Below 26 krpm, the total rotor orbital amplitudes are nearly negligible.

Figure 9 shows the rotor speed versus time. Rotors supported on gas bearings take long times to decelerate since the friction is small due to the gas film between the rotor and its bearings. In this case the rotor speed decays exponentially with time, denoting operations with "viscous" drag, On the other hand, operation with "dry friction" shows the speed decaying linearly with time and with a fast deceleration rate. The figure denotes three regimes of operation: *dry friction* from 50 krpm and 30 krpm as the rotor rubs on its bearings because of the large limit cycle motions; viscous drag from 30 krpm towards 5 krpm with a slow speed deceleration rate; and again *dry friction* from 5 krpm until rest and which lasts very little in time. Note that the region of *viscous drag* operation is the most desirable for rotors supported on gas bearings. The response with *dry friction* at low shaft speeds is unavoidable since the shaft speed is to low to warrant rotor lift off, i.e. generation of a hydrodynamic gas film. The operation with *rubbing* at high speeds is most undesirable due to the large frictional drag as well as the limit cycle motions of large amplitudes. Nonetheless, in spite of the exceedingly large rotor motions between 50 krpm and 26 krpm, the gas foil bearings are able to withstand these motions without major damage!

Coast down rotor response measurements for the rotor with added imbalance masses were not conducted because of fear of destroying the test bearings.

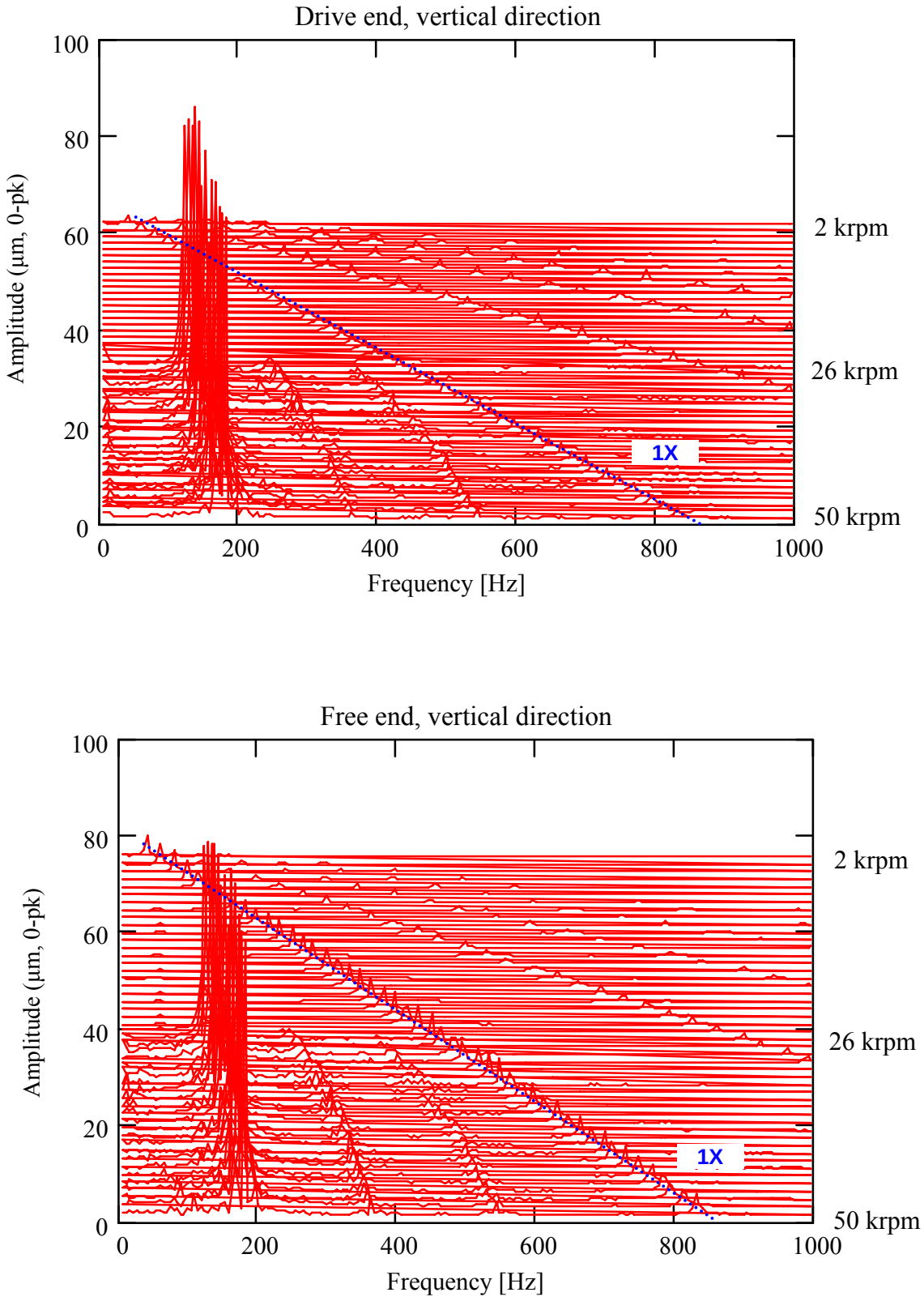

Figure 5. Waterfall of coast down rotor response from 50 krpm. Baseline imbalance condition, feed air pressure 34.5 kPa (5 psi). Vertical displacements at rotor drive and free ends

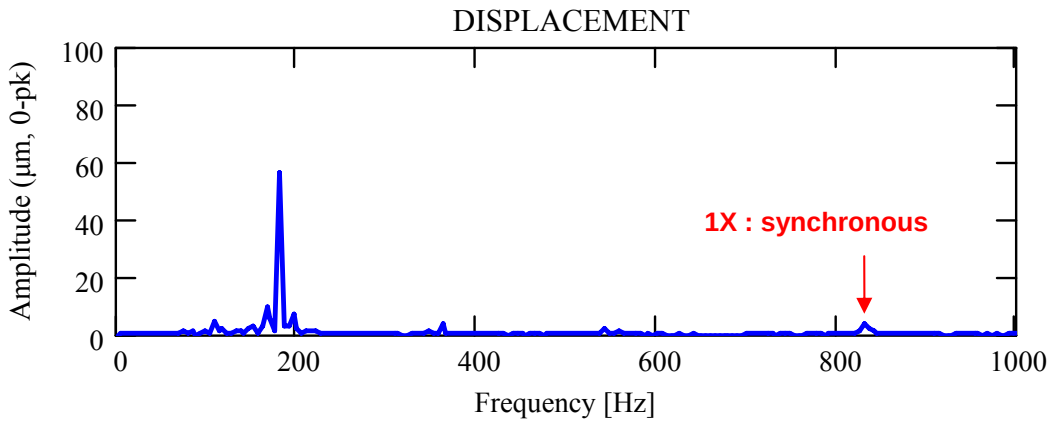

Figure 6. FFT spectrum of motion at rotor free end, vertical plane. Baseline imbalance condition, speed 50krm, air pressure at 34.5 kPa (5 psi)

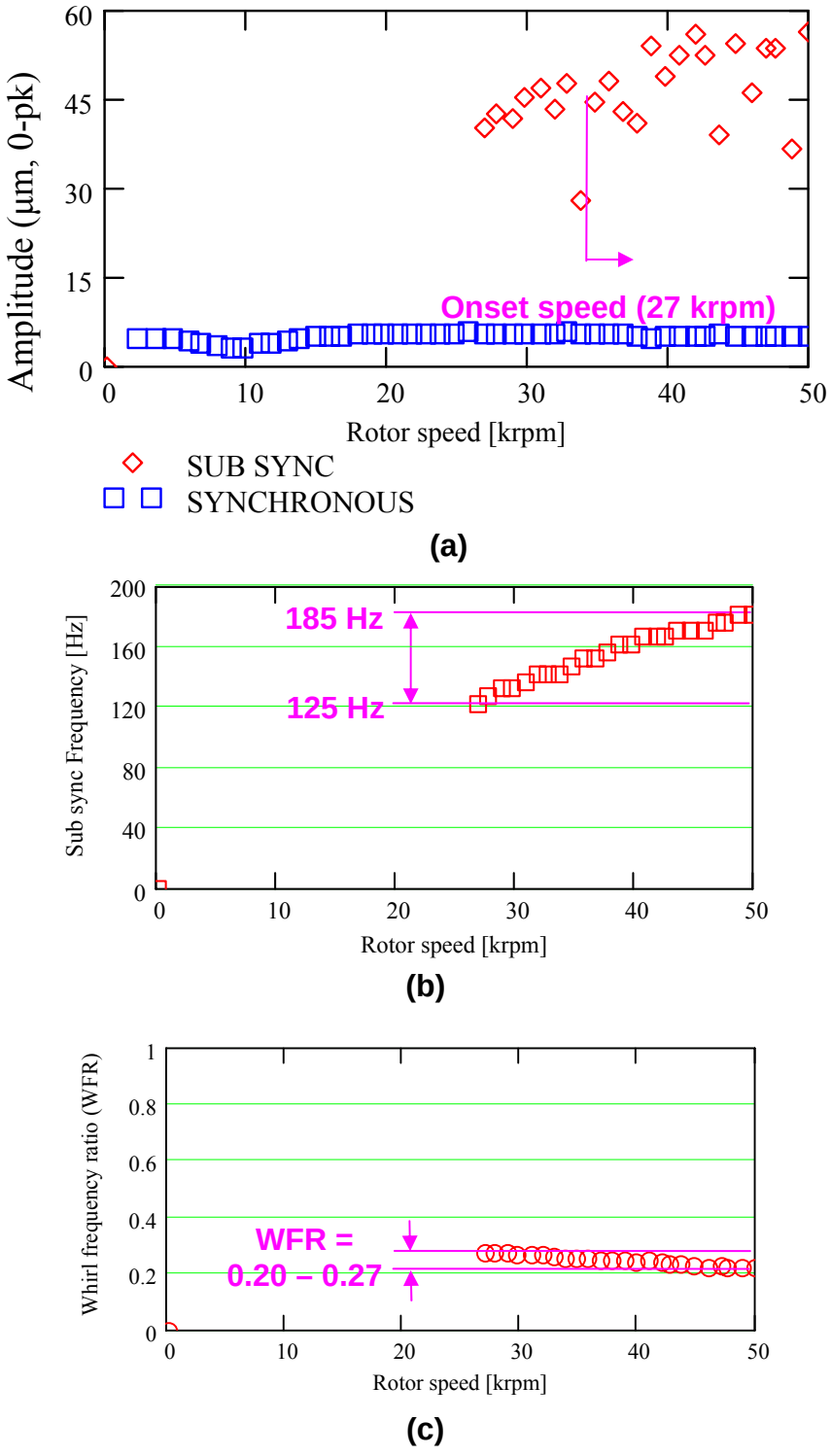

Figure 7. Analysis of whirl motions, amplitude and phase, versus rotor speed. (a) Amplitude of synchronous and subsynchronous rotor motions, (b) subsynchronous frequency, and (c) whirl frequency ratio. Baseline imbalance condition, air pressure 34.5 kPa (5 psi). Measurements at rotor free end, vertical plane

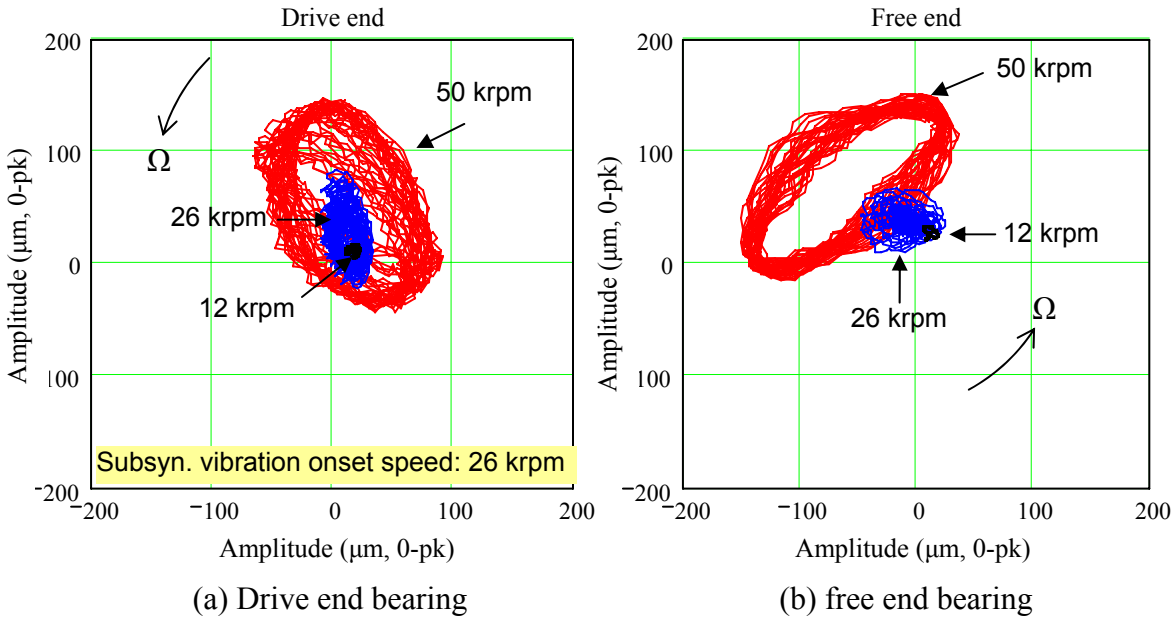

Figure 8. Rotor whirl orbits estimated at the bearing locations, drive and free ends. Baseline imbalance condition, feed air pressure at 34.5 kPa (5 psi). Orbits show DC-offset subtraction. Rotor speeds equal to 50, 26 and 12 krpm

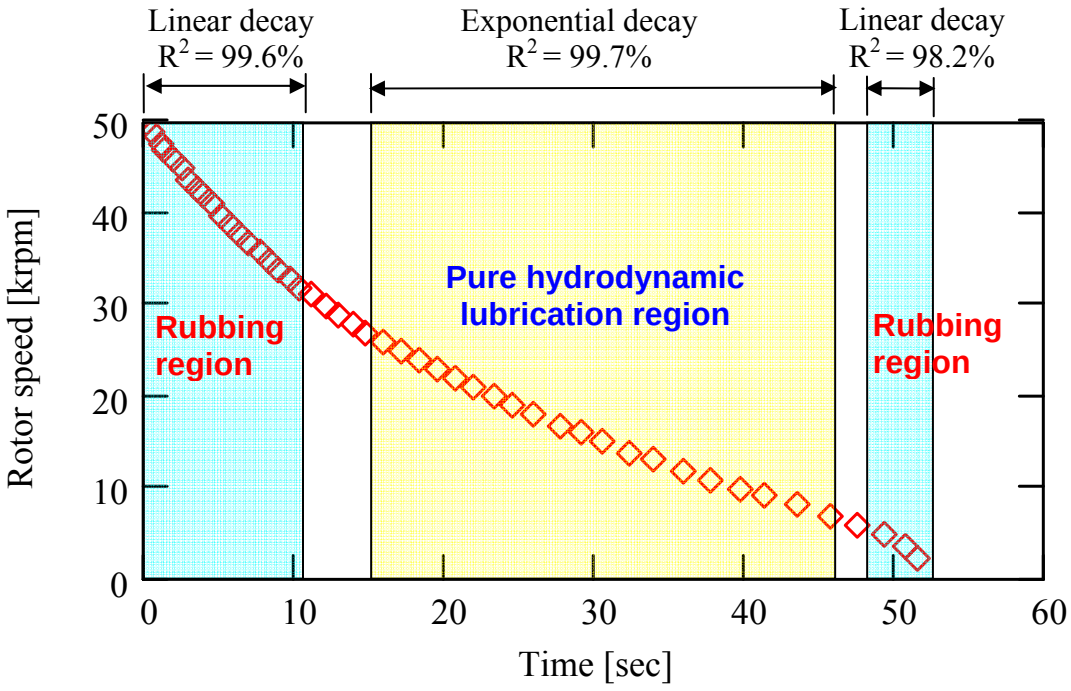

Figure 9. Rotor versus time during coast down test. Baseline imbalance condition. Air feed pressure at 34.5 kPa (5 psi)

IV.2 ROTOR COAST DOWN MEASUREMENTS FOR INCREASING MASS IMBALANCES

A number of tests were conducted with the rotor at its baseline condition and adding various imbalance masses. All measurements correspond to rotor coast downs from 25 krpm with air feed pressure at 34.5 kPa (5psi). In the following, acronyms for rotor responses are: DV and DH for drive bearing side, vertical and horizontal planes; and, FV and FH for free end bearing side.

For the baseline rotor condition, Figure 10 displays the amplitudes of total motion (direct) and synchronous motion, and phase angle versus rotor speed. The synchronous amplitude and phase angle denote subtraction of shaft run out at 2.5 krpm. The maximum direct and synchronous amplitudes are 12 μm and 8 μm, i.e. ~ < 27 % of the bearings nominal clearances. Note that there are not significant differences (< 1 μm) between the measurements at the rotor ends and the estimation of motions at the bearing locations because the measurements are taken near the bearings. No subsynchronous motions appear in the test speed range; however the FFT analysis does show small amplitudes of super-synchronous motions (2X, 3X), in particular at the drive end bearing locations; perhaps due to misalignment between the drive motor and rotor.

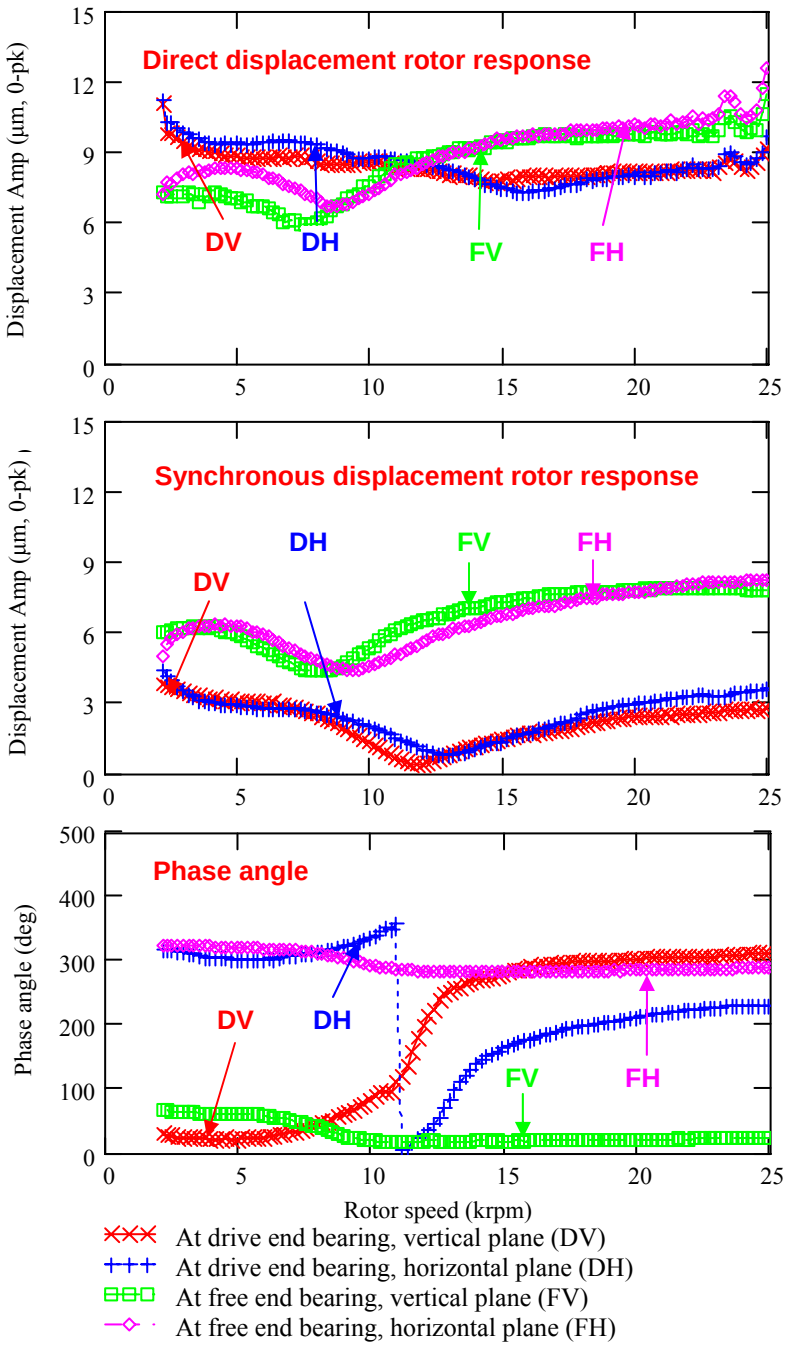

Figure 10. Baseline rotor response amplitudes (direct and synchronous) and phase angle versus shaft speed. Feed air pressure at 34.5 kPa (5 psi). Drive and end rotor ends, vertical and horizontal planes

Table 2 shows the imbalance masses added into the rotor end at radius (r) equal to 15.11 mm, the masses angular disposition (in-phase and out of phase 180º) as well as the equivalent imbalance displacements. The imbalance displacement, u, equals $u_i = m_e \times r/M_i$, $_{i=\text{drive end, free end}}$. The M_i mass parameters represent a fraction of the rotor weight (divided by gravity) acting on each bearing.

Table 2 Imbalance masses, equivalent imbalance displacements, and their location at rotor end planes

Imbalance test type		Imbalance mass (m_e)		Imbalance displacement (u)	
		Drive end	Free end	Drive end	Free end
In-phase	Test 1	55 mg (-45º)	55 mg (-45º)	1.26 μm	2.34 μm
	Test 2	110 mg (-45º)	110 mg (-45º)	2.52 μm	4.67 μm
	Test 3	165 mg (-45º)	165 mg (-45º)	3.78 μm	7.00 μm
Out-of-phase	Test 1	55 mg (-45º)	55 mg (135º)	1.26 μm	2.34 μm
	Test 2	110 mg (-45º)	110 mg (135º)	2.52 μm	4.67 μm
	Test 3	165 mg (-45º)	165 mg (135º)	3.78 μm	7.00 μm

(Bearing load: 0.66 kg_f and 0.36 kg_f for drive end and free end bearings, respectively. Coupling force not considered)

For general machinery, API recommends a maximum allowable imbalance U_{max} (oz.inch) $=4W/N$ [21], where W is the rotor weight in lb_f and N is rotor speed in rev/min (rpm). The calculated U_{max} for the test rotor at 10 krpm, near its critical speed, is 899.6×10^{-6} oz-inch (0.648 g-mm). Dividing U_{max} by the test rotor weight gives the maximum allowable imbalance displacement, u_{max}=0.635 μm. Note that the largest imbalance displacement measured during the baseline operation, presented in Fig. 10, is 12 μm, i.e., as large as 19 times u_{max}. This simple comparison implies that the test rotor should be balanced more for reliable operations in actual machinery. Note also that the API maximum allowable imbalance is perhaps impractical for small size rotors used in microturbomachinery.

Figures 11 and 12 depict the synchronous rotor response (amplitude and phase) for in-phase and out of phase imbalance masses, respectively. The measurements show the subtraction of the baseline synchronous response (amplitude and phase). The figures portray the vertical motions at the rotor drive and free ends.

The rotor amplitudes are well damped and increase as the imbalance masses increase. A critical speed is not discernible for the lowest imbalance masses. The phase angle is

practically invariant for all imbalance conditions. As the rotor speed increases towards 25 krpm, the amplitudes of imbalance response approach the in-phase imbalance displacements *(u)* shown in Table 2. For the out of phase imbalances, the amplitudes approach approximately two times the imbalance displacement (*u*). The critical speeds, determined at the phase angle of -90º range from 13 krpm to 10.5 krpm for in-phase imbalance masses, and 10 krpm to 9 krpm for out of phase imbalances. Appendix A presents the rotor synchronous responses, amplitude and phase angle, for measurements along the horizontal plane.

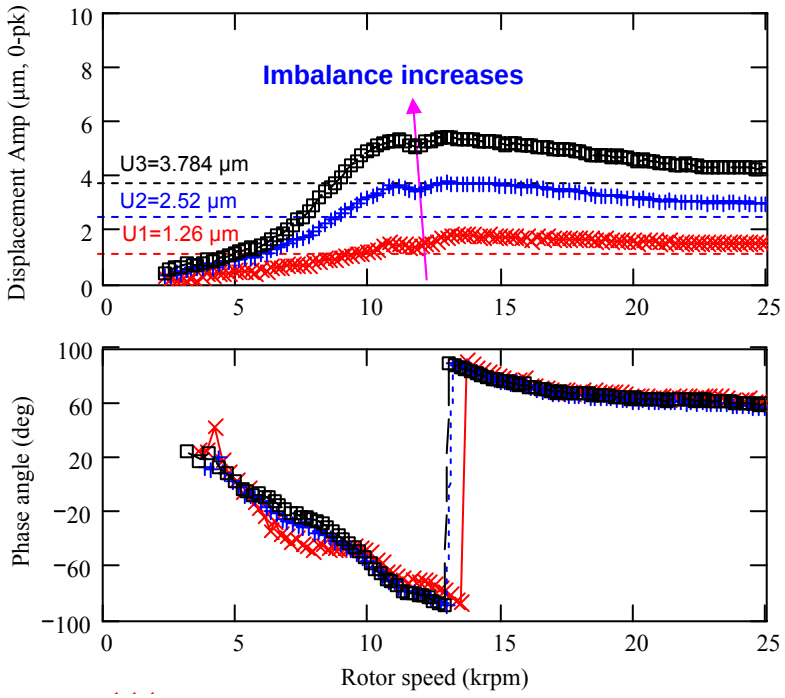

(a) Rotor drive end, vertical plane

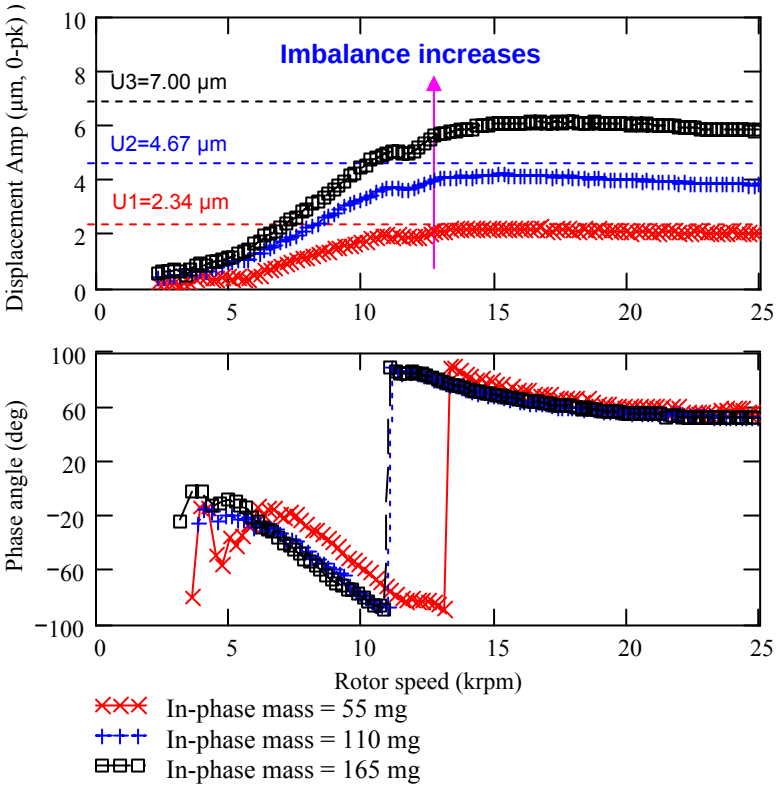

(b) Rotor free end, vertical plane

Figure 11. Amplitude and phase angle of synchronous rotor response for increasing in-phase imbalance masses. Measurements in vertical plane with baseline subtraction. Air supply at 34.4 kPa (5 psi)

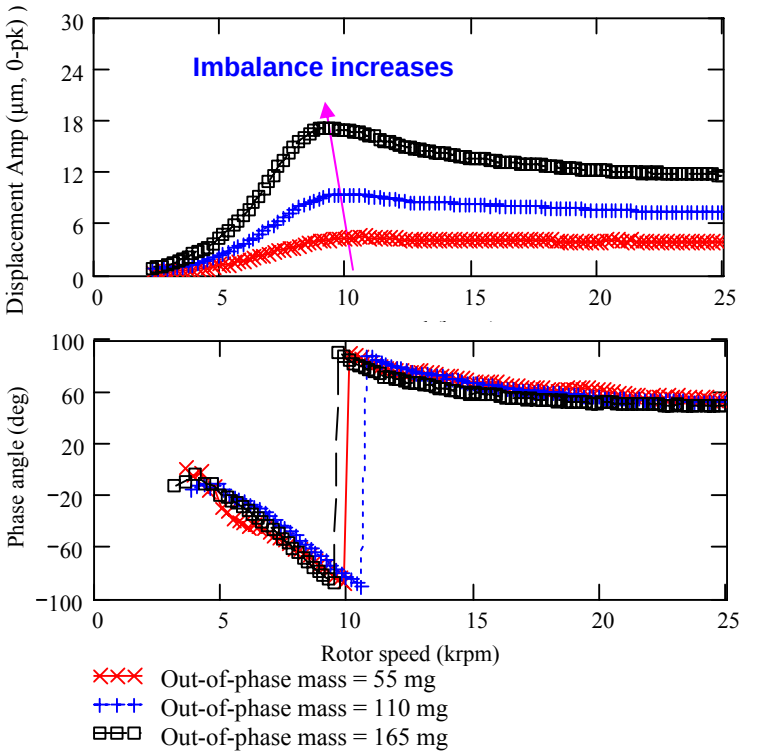

(a) Rotor drive end, vertical plane

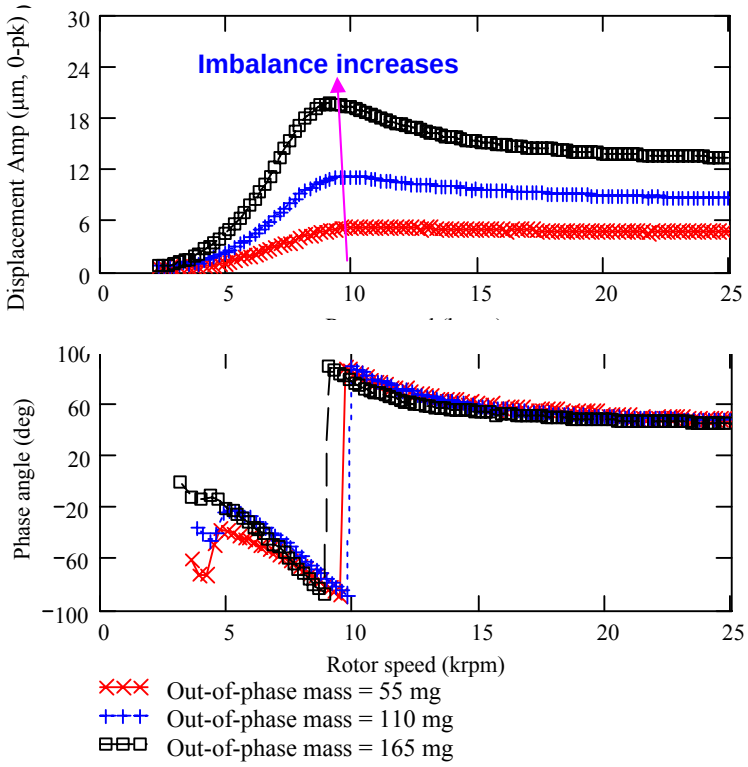

(b) Rotor free end, vertical plane

Figure 12. Amplitude and phase angle of synchronous rotor response for increasing out of phase imbalance masses. Measurements in vertical plane with baseline subtraction. Air pressure at 34.4 kPa (5 psi)

IV.3 RESPONSE LINEARITY OF ROTOR-GFBs SYSTEM

Figures 13 and 14 show normalized amplitudes of rotor synchronous response for in-phase and out-of-phase imbalance masses, respectively. The normalization procedure multiplies a recorded response by the ratio of smallest imbalance divided by the actual imbalance. For in-phase imbalance conditions, the test data evidence nearly uniform normalized amplitudes, i.e. characteristic of a linear system. The test data for out-of-phase imbalances show similar trends, except for the largest imbalance mass at rotor speed close to the system critical speed.

See Appendix B for the direct displacement rotor responses without baseline subtraction. The direct amplitudes increase significantly with out-of-phase imbalance masses, while they do not with in-phase imbalance masses. The maximum amplitude of direct rotor responses is ~25 μm, i.e., nearly half of the nominal bearing radial clearance (c=50 μm), at 9.3 krpm for the largest out-of-phase imbalance mass (m_e = 165 mg) and measurement at the free end bearing, vertical plane. Thus, the measurements imply that the original rotor has very large residual, out-of-phase imbalance.

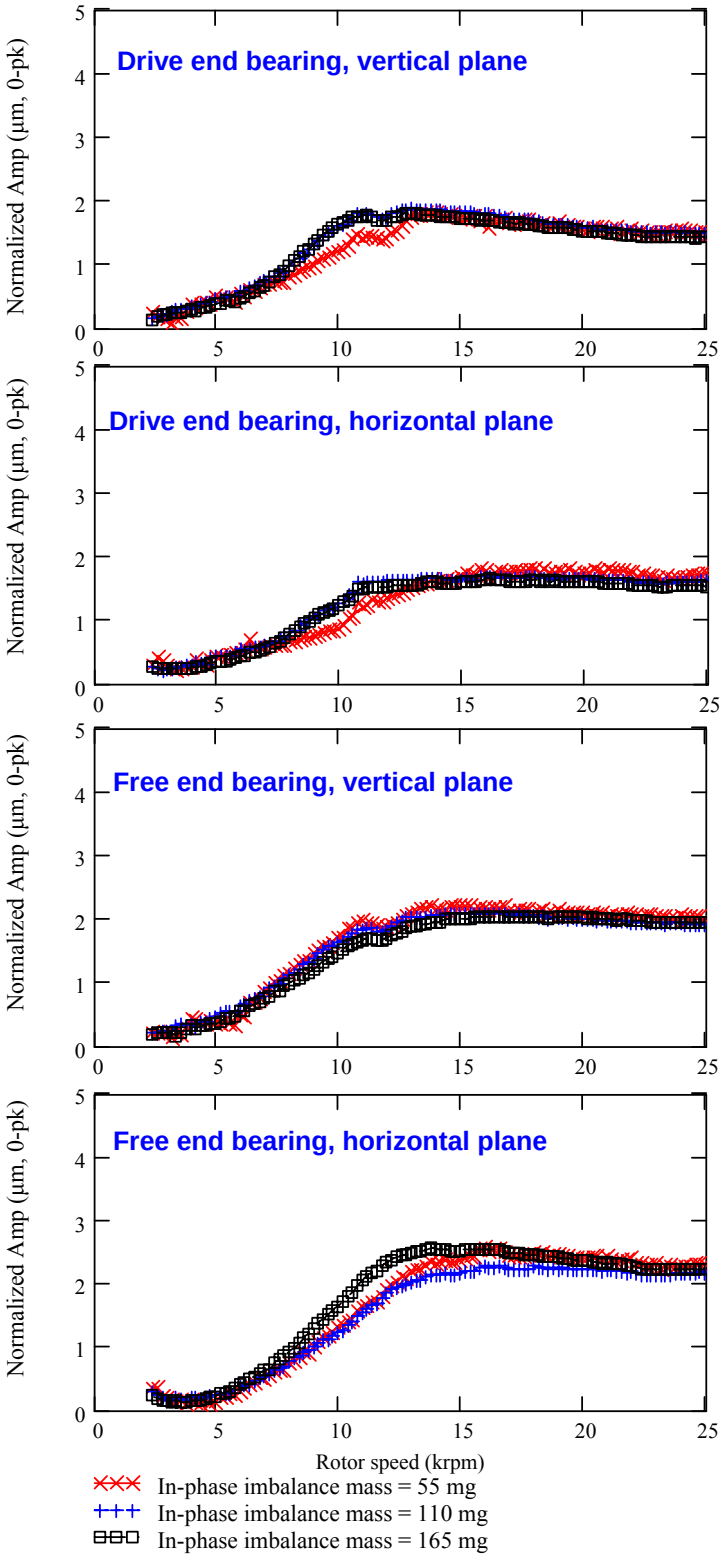

Figure 13. Normalized rotor amplitude of synchronous response for increasing in-phase imbalance mass. Baseline subtraction. Air supply pressure at 34.4 kPa (5psi).

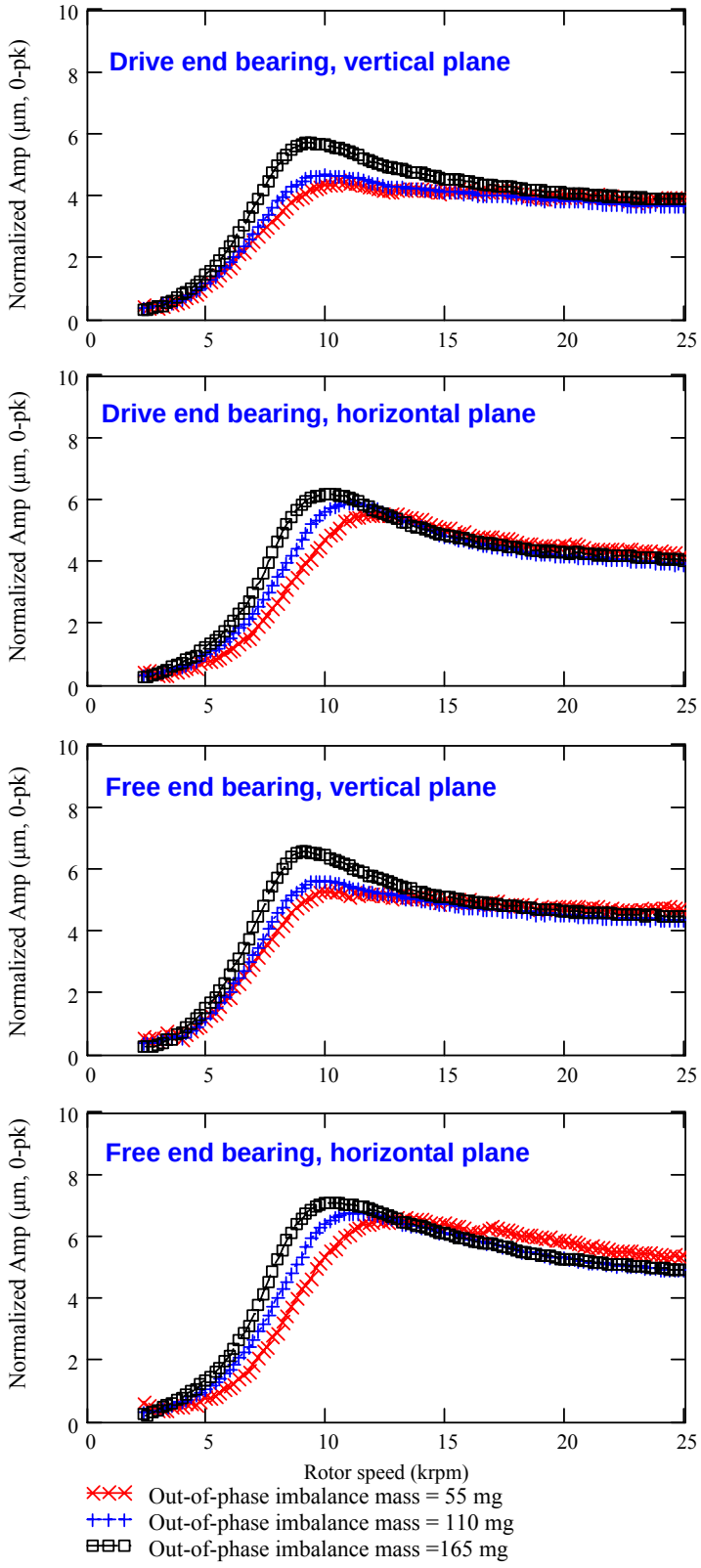

Figure 14. Normalized rotor amplitude of synchronous response for increasing out-of-phase imbalance mass. Baseline subtraction. Air supply pressure at 34.4 kPa (5psi).

V. CLOSURE

Further measurements of the dynamic motion response of a test rotor supported on bump-type gas foil bearings show a region of unstable performance at high shaft speeds. The measurements were conducted with side air feed pressurization at 5 psig into the test bearings. For the baseline condition (best balanced), coast down rotor responses from 50 krpm show significant subsynchronous motions between 50 krpm and 27 krpm, with whirl frequencies ranging from 20% to 27% of rotor speed. The large amplitude rotor motions, when operating with subsynchronous whirl, indicate the rotor rubs on its bearings from 50 krpm to 30 krpm.

Measurements of rotor motion for increasing mass imbalance conditions, in-phase and out-of-phase, are performed in coast downs from a top speed of 25 krpm to rest where no major subsynchronous vibrations exist. At the top rotor speed, the rotor amplitudes of synchronous motion approach the imbalance mass displacements. In general, the rotor coastdown responses for small imbalance masses show a linear rotor behavior with increasing rotor imbalance masses, implying that a rotordynamics model integrating linearized force coefficients for the gas foil bearings may predict accurately the rotor behavior. This observation is preliminary and further measurements will be conducted in the near future.

In spite of the large rotor motions recorded for speeds larger than 25 krpm when subsynchronous whirl sets in, the gas bearings appear to tolerate without damage the severe operating condition. Thus, the experiments conducted and observations inferred demonstrate that gas foil bearings are more rugged and reliable than other types of gas bearings operating under similar test conditions.

An increase in the test system natural frequency (ω_n) will raise the threshold speed of instability, i.e. $\Omega_{threshold} = \omega_n/WFR$. Therefore, further imbalance response tests will be conducted with foil bearings modified with shims inserted underneath the bump strips and in contact with the bearing housing. The shims will preload the bearings to increase their direct stiffnesses, thus rising the test system natural frequency and delaying the onset of subsynchronous whirl motions to higher shaft speeds. A companion TRC report [22] details the analysis of GFBs with mechanical preloads.

VI. REFERENCES

[1] Agrawal, G. L., 1997, "Foil Air/Gas Bearing Technology – an Overview," ASME paper 97-GT-347.

[2] Heshmat, H., and Hermel, P., 1993, "Compliant Foil Bearings Technology and Their Application to High Speed Turbomachinery," Thin Films in Tribology, pp. 559-575.

[3] San Andrés, L., 1995, "Turbulent Flow Foil Bearings for Cryogenic Applications," J. Tribol., **117**, pp. 185-195.

[4] Barnett, M. A., and Silver, A., 1970, "Application of Air Bearing to High-Speed Turbomachinery," SAE Paper No. 700720.

[5] Emerson, T. P., 1978, "The Application of Foil Air Bearing Turbomachinery in Aircraft Environmental Control Systems," ASME Paper No. 780-ENAS-18.

[6] Heshmat, C. A., Heshmat, H., 1995, "An Analysis of Gas-Lubricated, Multileaf Foil Journal Bearings with Backing Springs," J. Tribol., **117**, pp. 437-443.

[7] DellaCorte, C., and Valco, M. J., 2000, "Load Capacity Estimation of Foil Air Journal Bearings for Oil-Free Turbomachinery Applications," NASA/TM—2000-209782.

[8] Heshmat, H., 1994, "Advancements in the Performance of Aerodynamic Foil Journal Bearings: High Speed and Load Capacity," J. Tribol., **116**, pp. 287-295.

[9] Swanson, E. E., Heshmat, H., and Shin, J. S., 2002, "The Role of High Performance Foil Bearings in an Advanced, Oil-Free, Integral Permanent Magnet Motor Driven, High-Speed Turbo-Compressor Operating Above the First Bending Critical Speed," ASME Paper No. GT2002-30579.

[10] Oh, J., and Lee, H., 2003, "Development of High-Speed Industrial Turbo Blowers with Foil Air Bearings," ASME Paper No. GT2003-38606.

[11] Blok, H. and vanRossum, J. J., 1953, "The Foil Bearing – A New Departure In hydrodynamic Lubrication," Lubr. Eng., December, pp. 316-320.

[12] Ruscitto, D., Mc Cormick, J., and Gray, S., 1978, "Hydrodynamic Air Lubricated Compliant Surface Bearing For An Automotive Gas Turbine Engine I-Journal Bearing Performance," NASA CR-135368.

[13] Heshmat, H., Shapiro, W., and Gray, S., 1982, "Development of Foil Journal Bearings for High Load Capacity and High Speed Whirl Stability," J. lubr. Tech., **104**, pp. 149-156.

[14] Heshmat, H., 2000, "Operation of Foil Bearing Beyond the Bending Critical Mode," J. Tribol., **122**(1), pp. 192-198.

[15] Lee, Y.B., Kim, T.H., Kim, C.H., Lee, N.S., and Choi, D.H., 2004. "Dynamic Characteristics of a Flexible Rotor System Supported by a Viscoelastic Foil Bearing (VEFB)," Tribol. Intl., **37**, pp. 679-687.

[16] Howard, S., DellaCorte, C., Valco, M.-J., Prahl, J.-M., and Heshmat, H., 2001, "Dynamic Stiffness and Damping Characteristics of a High-Temperature Air Foil Journal Bearing," Tribol. Trans., **44** (4), pp. 657-663.

[17] San Andrés, L., Rubio, D., and Kim, T.H, 2006, "Rotordynamic Performance of a Rotor Supported on Bump Type Foil Gas Bearings: Experiments and Predictions," ASME Paper No. GT2006-91238.

[18] Dario, R., and San Andrés, L., 2005, "Rotordynamic Performance of a Rotor Supported on Gas Foil Bearings," Research Progress Report No. TRC-B&C-2-05, Turbomachinery Laboratory, Texas A&M University.

[19] Iordanoff, I., 1999, "Analysis of an Aerodynamic Compliant Foil Thrust Bearing: Method for a Rapid Design," ASME Journal of Tribology, **121**, pp 816-822.

[20] Vance, J. M., 1988, *Rotordynamics of Turbomachinery*, John Wiley & Sons, pp. 189-193.

[21] Standard Paragraphs, API Subcommittee on Mechanical Equipment, Revision 19, September 1991. American Petroleum Institute.

[22] San Andrés, L., and Kim, T., 2006, "Computational Analysis of Gas Foil Bearings Integrating 1D and 2D Finite Element Models for Top Foil," Annual Progress Report to Turbomachinery Research Consortium, TRC-B&C-1-06, Texas A&M University.

APPENDIX A. ROTOR SYNCHRONOUS RESPONSES (AMPLITUDE AND PHASE ANGLE) FOR INCREASING IMBALANCES. MEASUREMENTS AT ROTOR ENDS, HORIZONTAL PLANE

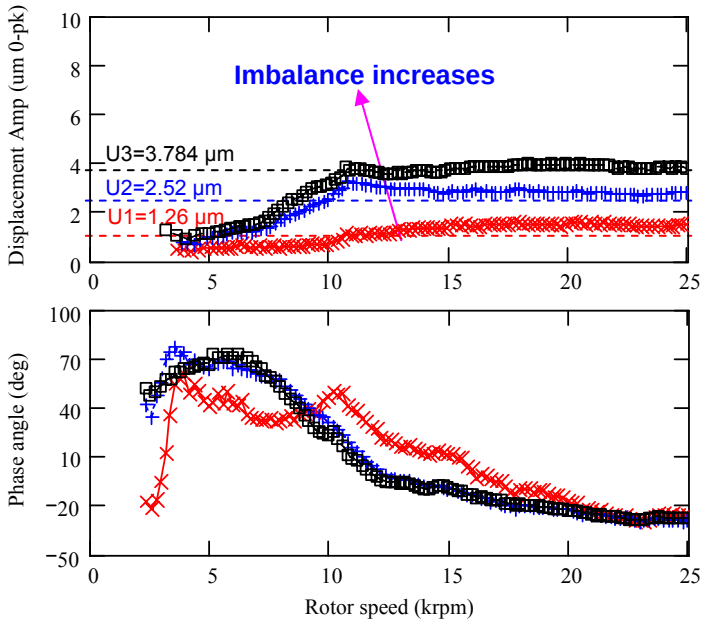

(a) Drive rotor end, horizontal plane

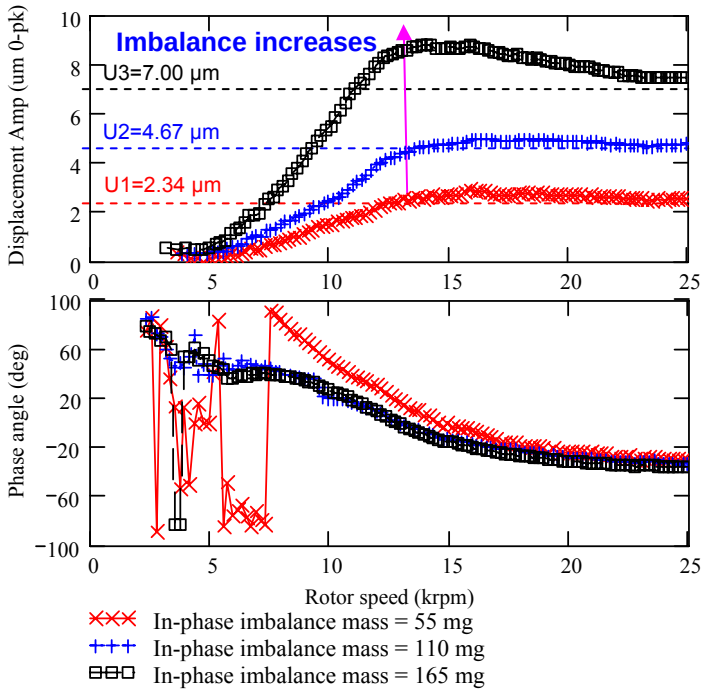

(b) Rotor free end, horizontal plane

Figure A1. Amplitude and phase angle of synchronous rotor response for increasing in-phase imbalance masses. Measurements in horizontal plane with baseline subtraction. Air pressure at 34.4 kPa (5 psi)

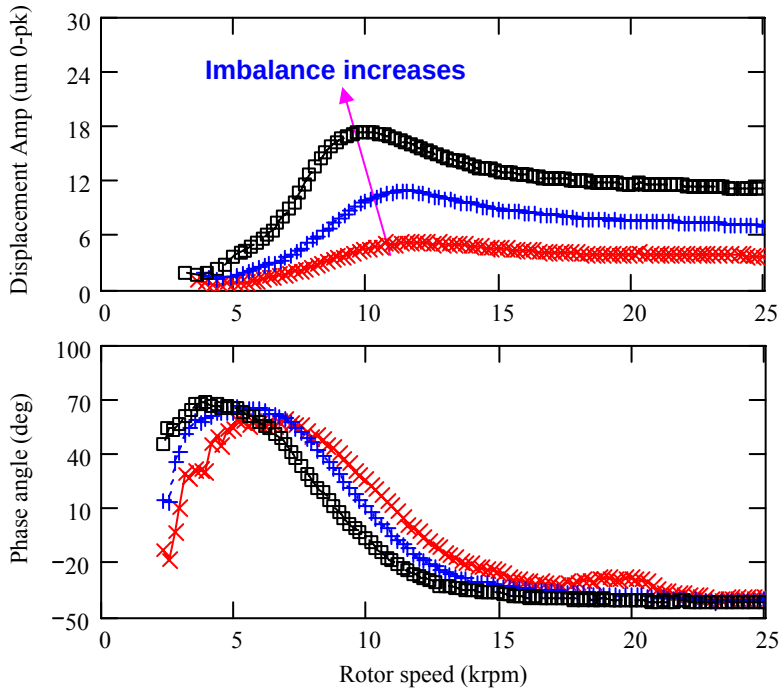

(a) Drive rotor end, horizontal plane

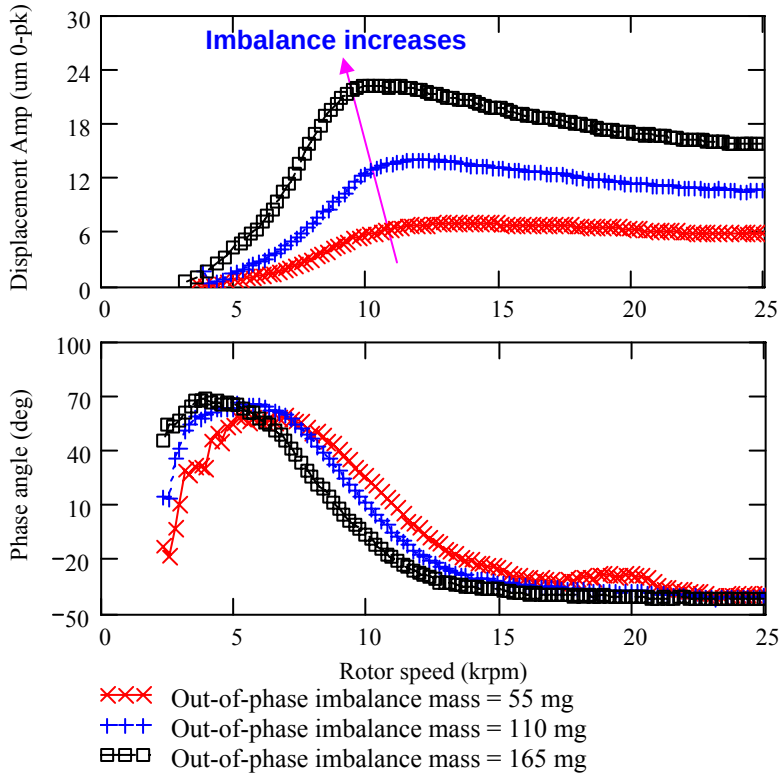

(b) Rotor free end, horizontal plane

Figure A2. Amplitude and phase angle of synchronous rotor response for increasing out of phase imbalance masses. Measurements in horizontal plane with baseline subtraction. Air pressure at 34.4 kPa (5 psi)

APPENDIX B. DIRECT DISPLACEMENT RESPONSE OF ROTOR WITHOUT BASELINE SUBTRACTION FOR INCREASING IMBALANCE MASSES

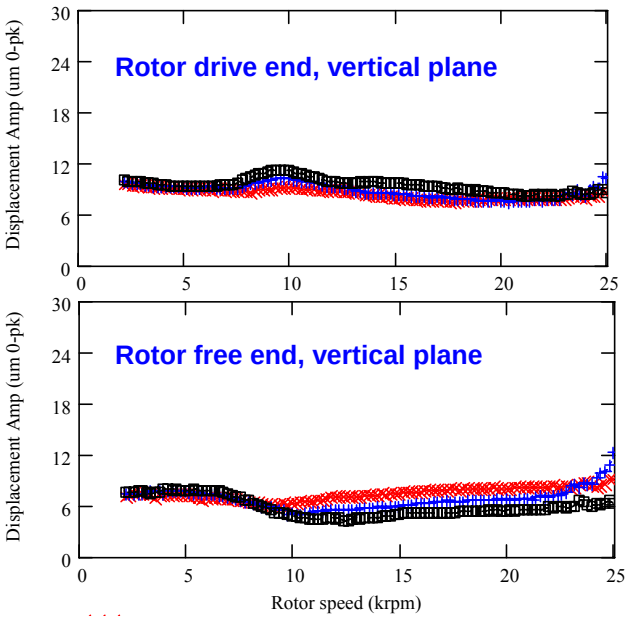

(a) In-phase imbalance test

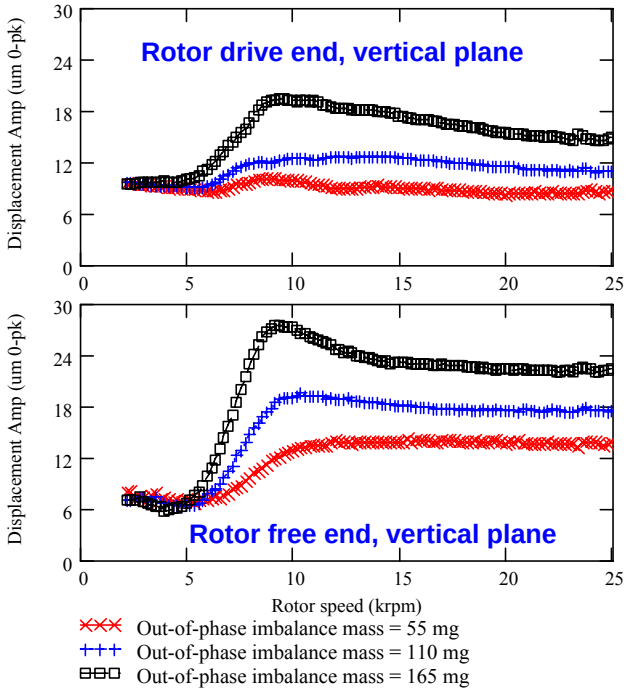

(b) Out-of-phase imbalance test

Figure B1. Direct displacement response of the rotor without baseline subtraction for increasing imbalance masses. Air pressure at 34.5 kPa (5 psi).